

JWST/NIRSpec Measurements of the Relationships Between Nebular Emission-line Ratios and Stellar Mass at $z \sim 3 - 6$

ALICE E. SHAPLEY,¹ NAVEEN A. REDDY,² RYAN L. SANDERS,^{3,*} MICHAEL W. TOPPING,⁴ AND GABRIEL B. BRAMMER^{5,6}

¹Department of Physics & Astronomy, University of California, Los Angeles, 430 Portola Plaza, Los Angeles, CA 90095, USA

²Department of Physics & Astronomy, University of California, Riverside, 900 University Avenue, Riverside, CA 92521, USA

³Department of Physics and Astronomy, University of California, Davis, One Shields Ave, Davis, CA 95616, USA

⁴Steward Observatory, University of Arizona, 933 N Cherry Avenue, Tucson, AZ 85721, USA

⁵Cosmic Dawn Center (DAWN), Denmark

⁶Niels Bohr Institute, University of Copenhagen, Lyngbyvej 2, DK2100 Copenhagen Ø, Denmark

ABSTRACT

We analyze the rest-optical emission-line ratios of star-forming galaxies at $2.7 \leq z < 6.5$ drawn from the Cosmic Evolution Early Release Science (CEERS) Survey, and their relationships with stellar mass (M_*). Our analysis includes both line ratios based on the $[\text{NII}]\lambda 6583$ feature – $[\text{NII}]\lambda 6583/\text{H}\alpha$, $([\text{OIII}]\lambda 5007/\text{H}\beta)/([\text{NII}]\lambda 6583/\text{H}\alpha)$ (O3N2), and $[\text{NII}]\lambda 6583/[\text{OII}]\lambda 3727$ – and those those featuring α elements – $[\text{OIII}]\lambda 5007/\text{H}\beta$, $[\text{OIII}]\lambda 5007/[\text{OII}]\lambda 3727$ (O₃₂), $([\text{OIII}]\lambda\lambda 4959, 5007+[\text{OII}]\lambda 3727)/\text{H}\beta$ (R₂₃), and $[\text{NeIII}]\lambda 3869/[\text{OII}]\lambda 3727$. Given the typical flux levels of $[\text{NII}]\lambda 6583$ and $[\text{NeIII}]\lambda 3869$, which are undetected in the majority of individual CEERS galaxies at $2.7 \leq z < 6.5$, we construct composite spectra in bins of M_* and redshift. Using these composite spectra, we compare the relationships between emission-line ratios and M_* at $2.7 \leq z < 6.5$ with those observed at lower redshift. While there is significant evolution towards higher excitation (e.g., higher $[\text{OIII}]\lambda 5007/\text{H}\beta$, O₃₂, O3N2), and weaker nitrogen emission (e.g., lower $[\text{NII}]\lambda 6583/\text{H}\alpha$ and $[\text{NII}]\lambda 6583/[\text{OII}]\lambda 3727$) between $z \sim 0$ and $z \sim 3$, we find in most cases that there is no significant evolution in the relationship between line ratio and M_* beyond $z \sim 3$. The $[\text{NeIII}]\lambda 3869/[\text{OII}]\lambda 3727$ ratio is anomalous in showing evidence for significant elevation at $4.0 \leq z < 6.5$ at fixed mass, relative to $z \sim 3.3$. Collectively, however, our empirical results suggest no significant evolution in the mass-metallicity relationship at $2.7 \leq z < 6.5$. Representative galaxy samples and metallicity calibrations based on existing and upcoming *JWST*/NIRSpec observations will be required to translate these empirical scaling relations into ones tracing chemical enrichment and gas cycling, and distinguish among descriptions of feedback in galaxy-formation simulations at $z > 3$.

1. INTRODUCTION

The rest-frame optical nebular emission-line spectrum of star-forming galaxies is rich with information probing their gas, heavy elements, dust, and massive stars. The pattern of rest-optical emission lines is also known to vary systematically as a function of stellar mass, (M_*). This variation occurs primarily as a result of the dependence of galaxy metallicity on galaxy stellar mass. This so-called “mass-metallicity relation” (MZR) has been traced using vast samples in the local universe drawn from the Sloan Digital Sky Survey (SDSS; e.g., Tremonti et al. 2004; Andrews & Martini 2013), and, with smaller, yet still statistical, power all the way out to $z \sim 3$ (e.g., Onodera et al. 2016; Kashino et al. 2017; Topping et al. 2021; Sanders et al. 2021). A secondary,

additional dependence of metallicity on star-formation rate (SFR) has been discovered as well (e.g., Ellison et al. 2008; Mannucci et al. 2010), the “Fundamental Metallicity Relation,” (FMR) which appears not to evolve significantly between $z \sim 0$ and $z \sim 3$ (Sanders et al. 2021).

Previously restricted to $z \lesssim 3.5$, studies of the rest-optical emission-line properties of star-forming galaxies can now be extended deep into the reionization epoch with *JWST*. Even the very first NIRSpec spectroscopic data released to the public revealed the promise of *JWST* for estimating the gas-phase chemical abundances of star-forming galaxies at $z \sim 7.5 - 8.5$ (e.g., Arellano-Córdova et al. 2022; Curti et al. 2023). Subsequent remarkable NIRSpec spectra have revealed the rest-optical nebular properties of individual galaxies at $z = 9.5$ (Williams et al. 2022), and, now, $z = 10.6$ (Bunker et al. 2023). The low metallicities of the $z > 8$ targets observed by *JWST*, given their stellar masses and SFRs, suggest that they do not fall on the FMR that describes galaxies at $z \leq 3$ (Curti et al. 2023; Williams et al. 2022; Langeroodi et al. 2022).

aes@astro.ucla.edu

* NHFP Hubble Fellow

However, it is challenging to draw broad conclusions from such a small sample, which may or may not be representative of the full population at these redshifts, and questions remain about which calibrations can be used to accurately infer metallicity at such high redshifts.

Larger samples are clearly needed to place detailed, single-object results in context. The CEERS Early Release Science program (Finkelstein et al. 2023, 2022, ; Finkelstein et al., in prep.) provides one of the first such opportunities (see also Matthee et al. 2022; Mascia et al. 2023; Cameron et al. 2023), including 6 NIRSpec pointings in the EGS field using the medium resolution ($R \sim 1000$) grating, and 6 pointings using the $R \sim 100$ prism, targeting collectively ~ 1000 galaxies with photometric redshifts over the range $z \sim 0.5 - 12$ (Fujimoto et al. 2023). Already, CEERS is providing a window into the excitation properties of star-forming galaxies out to $z \sim 9$ (Sanders et al. 2023b; Tang et al. 2023). Even $z \sim 3.5 - 6.5$ represents uncharted territory for rest-optical spectroscopic emission-line studies of star-forming galaxies. Furthermore, *JWST*/NIRSpec provides access to a broader complement of rest-optical emission lines at $z \sim 3.5 - 6.5$ than those covered for the most distant galaxies with *JWST* spectra (Shapley et al. 2023). Based on its richness, with simultaneous coverage of $[\text{OII}]\lambda 3727$, $[\text{NeIII}]\lambda 3869$, $\text{H}\beta$, $[\text{OIII}]\lambda\lambda 4959, 5007$, $\text{H}\alpha$, and $[\text{NII}]\lambda 6583$ in CEERS/NIRSpec medium-resolution spectra, we focus in this work on the redshift range $z = 2.7 - 6.5$. Robust stellar mass estimates for galaxies in this redshift range enable us to analyze the relationships among rest-optical emission-line ratios and stellar masses. Tracing these relationships for both α -elements (e.g., O, Ne) and nitrogen is a first crucial step towards establishing metallicity scaling relationships at $z > 3$, which also requires a robust calibration between emission-line properties and oxygen abundance (Bian et al. 2018; Sanders et al. 2020, 2021; Nakajima et al. 2023).

In §2, we describe observations and samples analyzed here. In §3, we present results on the observed relationships between rest-optical emission-line ratios and stellar mass, measured continuously from $z \sim 3 - 6$. In §4, we compare with other recent work and consider the implications of these new measurements for the evolution of metallicity scaling relations among galaxies. Throughout, we adopt cosmological parameters of $H_0 = 70 \text{ km s}^{-1} \text{ Mpc}^{-1}$, $\Omega_m = 0.3$, and $\Omega_\Lambda = 0.7$, and a Chabrier (2003) IMF.

2. OBSERVATIONS, SAMPLE, AND MEASUREMENTS

2.1. *Observations*

Our analysis is based on the public NIRSpec Micro-Shutter Assembly (MSA) data from the CEERS program (Program ID:1345; Finkelstein et al. 2023, 2022, ; Arrabal Haro et al., in prep.). We analyze data from 6 medium-resolution ($R \sim 1000$) NIRSpec pointings in the AEGIS

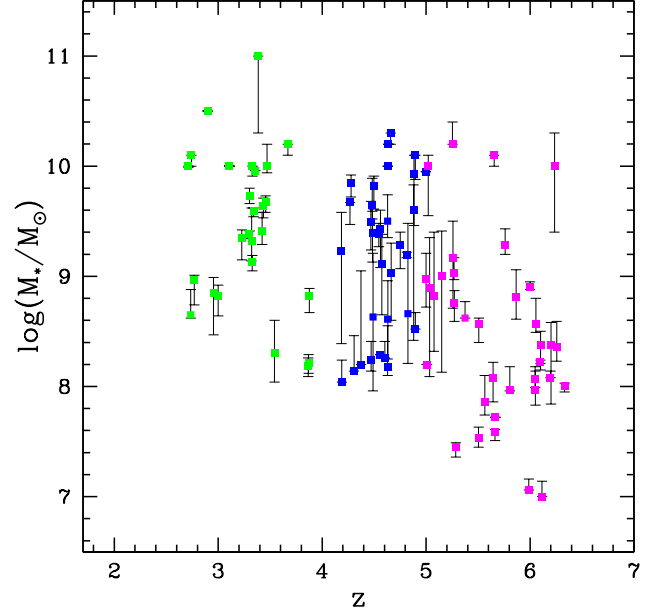


Figure 1. Stellar mass vs. redshift for all 94 CEERS galaxies at $2.7 \leq z \leq 6.5$ analyzed in this work. Galaxies at $z = 2.7 - 4.0$ are color-coded green; those at $z = 4.0 - 5.0$ are shown in blue; finally, those at $z = 5.0 - 6.5$ are indicated in magenta.

field, spanning $1 - 5 \mu\text{m}$ with the grating/filter combination of G140M/F100LP, G235M/F170LP, and G395M/F290LP. These 6 pointings included a total sample of 318 distinct targets, observed for 3107 seconds in each grating/filter combination. Two-dimensional (2D) data processing steps, one-dimensional (1D) extraction, slit-loss corrections, band-to-band flux calibration, and the measurement of emission-line fluxes are all described in detail in Shapley et al. (2023), Sanders et al. (2023b), and Reddy et al. (2023).

We extracted spectra for 252 CEERS targets, and measured spectroscopic redshifts for 231. As described in Shapley et al. (2023), we modeled existing *HST*/ACS and WFC3, *JWST*/NIRCam, *Spitzer*/IRAC, and ground-based photometry for CEERS galaxy targets using the FAST program (Kriek et al. 2009), assuming the stellar population synthesis models of Conroy et al. (2009). We adopted delayed- τ star-formation histories, where $SFR(t) \propto t \times \exp(-t/\tau)$, and t is the time since the onset of star formation. Robust spectral energy distributions (SEDs), corrected for emission-line fluxes, were determined for 210 of the 231 galaxies with spectroscopic redshifts, for which we accordingly obtained stellar mass estimates.

2.2. *Sample*

We restricted the current analysis to CEERS galaxies at $2.7 \leq z < 6.5$, which spans in redshift from the current ground-based high-redshift limit for $\text{H}\alpha$ measurements, up to the limit at which $\text{H}\alpha$ and $[\text{NII}]\lambda 6583$ can be measured

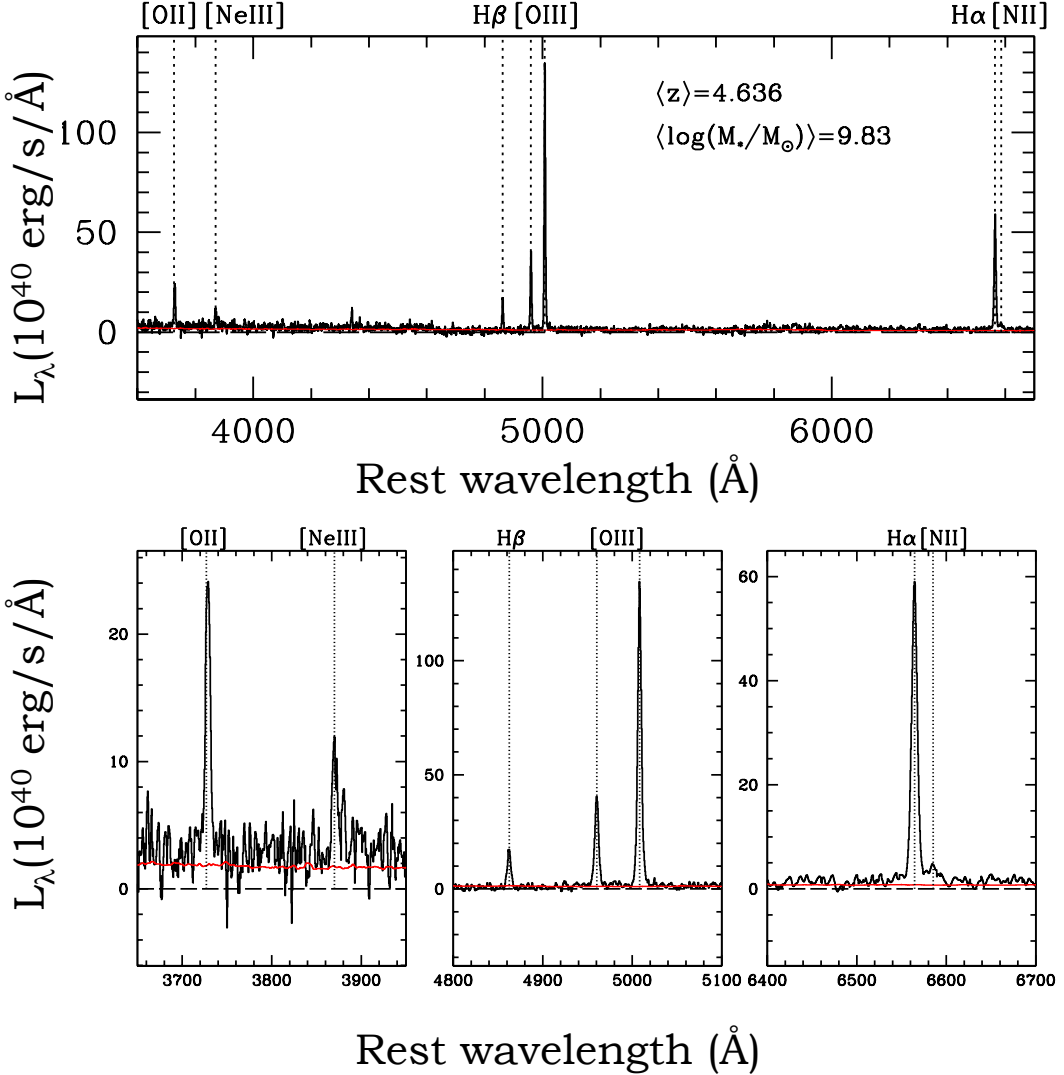


Figure 2. Composite spectrum of the high-mass bin of CEERS galaxies at $z = 4.0 - 5.0$. The composite spectrum is indicated with a black curve, while the error spectrum is shown in red. In the top row, the full composite spectrum is shown, along with the mean redshift and stellar mass. The bottom row includes three zoomed-in regions covering the vicinity of the key nebular lines analyzed in this work. These emission lines are labeled and marked with vertical dotted lines in both full and zoomed-in spectral panels.

with the NIRSpec G395M/F290LP set-up. We also require an estimate of stellar mass, and a lack of spectroscopic indication of active galactic nucleus (AGN) activity, such as $\log([NII]\lambda 6583/H\alpha) \geq -0.3$ or broad $H\alpha$ emission. These criteria yield a sample of 94 galaxies. In order to search for redshift evolution, we construct three redshift subsamples at $2.7 \leq z < 4$ (27 galaxies), $4.0 \leq z < 5.0$ (32 galaxies), and $5.0 \leq z < 6.5$ (35 galaxies). In Figure 1, we plot the stellar masses and redshifts for our sample, color-coded according to redshift. In Shapley et al. (2023), we showed that the $2.7 \leq z < 4.0$ and $4.0 \leq z < 5.0$ CEERS samples are representative of main sequence star-forming galaxies (Speagle et al. 2014), whereas the $5.0 \leq z < 6.5$ may represent galaxies with higher than average specific SFRs.

2.3. Measurements

Based on the emission-line measurements from CEERS galaxy spectra, we estimated several line ratios for each galaxy, which form the basis of our analysis. These line ratios include:

- $[NII]\lambda 6583/H\alpha$
- $([OIII]\lambda 5007/H\beta)/([NII]\lambda 6583/H\alpha)$ (hereafter O3N2)
- $[NII]\lambda 6583/[OII]\lambda 3727$
- $[OIII]\lambda 5007/H\beta$
- $[OIII]\lambda 5007/[OII]\lambda 3727$ (hereafter O₃₂)
- $([OIII]\lambda 5007+[OII]\lambda 3727)/H\beta$ (hereafter R₂₃)
- $[NeIII]\lambda 3869/[OII]\lambda 3727$

Ratios between lines with small wavelength separation (i.e., $[NII]\lambda 6583/H\alpha$, O3N2, $[OIII]\lambda 5007/H\beta$,

Table 1. Emission-line Properties of CEERS Composite Spectra

			$\log\left(\frac{M_*}{M_\odot}\right)$ ^a	N^b	$\log\left(\frac{[\text{NII}]}{\text{H}\alpha}\right)$	$\log(\text{O3N2})$	$\log\left(\frac{[\text{NII}]}{[\text{OII}]}\right)$	$\log\left(\frac{[\text{OIII}]}{\text{H}\beta}\right)$	$\log(\text{O}_{32})$	$\log(\text{R}_{23})$	$\log\left(\frac{[\text{NeIII}]}{[\text{OII}]}\right)$
$z = 2.7 - 4.0$ stacks in bins of M_*											
8.93 ± 0.13	12	$-1.48^{+0.07}_{-0.08}$	$2.26^{+0.07}_{-0.08}$		$-1.28^{+0.08}_{-0.09}$	$0.78^{+0.01}_{-0.01}$		$0.54^{+0.02}_{-0.03}$	$0.99^{+0.01}_{-0.02}$	$-0.41^{+0.03}_{-0.03}$	
10.09 ± 0.10	13	$-0.88^{+0.01}_{-0.01}$	$1.36^{+0.02}_{-0.02}$		$-0.90^{+0.03}_{-0.03}$	$0.48^{+0.01}_{-0.01}$		$0.01^{+0.02}_{-0.02}$	$0.84^{+0.02}_{-0.02}$	$-1.25^{+0.10}_{-0.12}$	
$z = 4.0 - 5.0$ stacks in bins of M_*											
8.76 ± 0.15	13	$-1.46^{+0.08}_{-0.09}$	$2.24^{+0.08}_{-0.10}$		$-1.30^{+0.09}_{-0.11}$	$0.78^{+0.03}_{-0.03}$		$0.48^{+0.04}_{-0.04}$	$0.99^{+0.03}_{-0.04}$	$-0.38^{+0.04}_{-0.04}$	
9.83 ± 0.08	13	$-1.23^{+0.03}_{-0.03}$	$2.04^{+0.03}_{-0.03}$		$-1.17^{+0.04}_{-0.05}$	$0.81^{+0.01}_{-0.02}$		$0.40^{+0.02}_{-0.02}$	$1.02^{+0.02}_{-0.02}$	$-0.55^{+0.05}_{-0.05}$	
$z = 5.0 - 6.5$ stacks in bins of M_*											
7.98 ± 0.11	16	$-1.36^{+0.09}_{-0.11}$	$2.15^{+0.09}_{-0.11}$		$-1.23^{+0.10}_{-0.13}$	$0.78^{+0.02}_{-0.02}$		$0.45^{+0.06}_{-0.07}$	$0.99^{+0.02}_{-0.02}$	$-0.53^{+0.14}_{-0.20}$	
9.25 ± 0.15	15	$-1.31^{+0.05}_{-0.06}$	$1.99^{+0.05}_{-0.06}$		$-1.07^{+0.06}_{-0.07}$	$0.69^{+0.01}_{-0.02}$		$0.47^{+0.02}_{-0.02}$	$0.90^{+0.02}_{-0.02}$	$-0.49^{+0.06}_{-0.07}$	

^a Median stellar mass of galaxies in each bin. ^b Number of galaxies in each bin. The composite sample includes a total of 82 galaxies with H α detections.

[NeIII] $\lambda 3869$ /[OII] $\lambda 3727$) do not require corrections for dust attenuation, and are presented as is, while [NII] $\lambda 6583$ /[OII] $\lambda 3727$, O₃₂, and R₂₃ are corrected for dust attenuation based on the H α /H β Balmer decrement, assuming an intrinsic H α /H β ratio of 2.79 and the Cardelli et al. (1989) dust law, which has been shown to be appropriate for high-redshift star-forming galaxies (Reddy et al. 2020).

While the majority of our sample has individual detections of [OIII] $\lambda 5007$ /H β , O₃₂, and R₂₃, any line ratio including either [NII] or [NeIII] results in a majority of limits in either one or more required emission lines. In order to utilize the full sample, including limits, and obtain results that are representative of the relationships between emission-line ratios and stellar mass, we constructed composite spectra in two roughly equal-sized bins of stellar mass for each of the three redshift bins. The 82 (out of 94) CEERS galaxies at $2.7 \leq z < 6.5$ with detections of H α were included in the sample for stacking. H α detections were required since individual spectra were normalized to a common H α luminosity before averaging. Emission line fluxes, ratios, and uncertainties were measured from each composite spectrum (Reddy et al. 2023). Figure 2 shows an example of a CEERS composite spectrum, representing the high-mass bin within the redshift range $z = 4.0 - 5.0$. All key emission lines used in our analysis are labeled.

3. RESULTS

We present the relations between emission-line ratios and stellar mass in each of the three CEERS redshift bins spanning $2.7 \leq z < 6.5$. We plot individual CEERS galaxies when a detection or meaningful 3 σ upper- or lower-limit

can be derived. Given the low detection rate for some line ratios, we also plot values measured from composite spectra in two bins of stellar mass for each redshift bin. These values are presented in Table 1. For comparison, we indicate the analogous relations for lower-redshift samples. Specifically, in all panels, we plot the distribution of SDSS $z \sim 0$ star-forming galaxies as a grey, 2D histogram (Abazajian et al. 2009). We also plot measurements from stacked spectra of star-forming galaxies drawn from the MOSDEF survey. These include $z \sim 1.5$ measurements from Topping et al. (2021), and $z \sim 2.3$ and $z \sim 3.3$ measurements from Sanders et al. (2021). The $z \sim 2.3$ measurements span [OII] $\lambda 3727$, [NeIII] $\lambda 3869$, H β , [OIII] $\lambda 5007$, H α , and [NII] $\lambda 6583$, whereas the $z \sim 1.5$ measurements lack the bluest features ([OII] $\lambda 3727$, [NeIII] $\lambda 3869$); conversely, the $z \sim 3.3$ measurements lack the reddest features (H α and [NII] $\lambda 6583$).

3.1. Line Ratios Including Nitrogen

We begin with scaling relations including the [NII] $\lambda 6583$ line: [NII] $\lambda 6583$ /H α , O₃₂, and [NII] $\lambda 6583$ /[OII] $\lambda 3727$. One basic result concerns the relative faintness of [NII] $\lambda 6583$. Out of 82 galaxies with coverage of both [NII] $\lambda 6583$ and H α at $z = 2.7 - 6.5$, only 31 have 3 σ detections of [NII] $\lambda 6583$. The CEERS composite spectra show that the typical ratio of [NII] $\lambda 6583$ /H α in this redshift range is 0.04–0.06, except at $\log(M_*/M_\odot) \geq 10$, where it rises to 0.10–0.15 in the lowest-redshift bin. Indeed, based on both individual datapoints and stacked measurements, there is evidence in Figure 3 (left) for a scaling between [NII] $\lambda 6583$ /H α and M_{*} within the CEERS $z = 2.7 - 4.0$ bin, which is con-

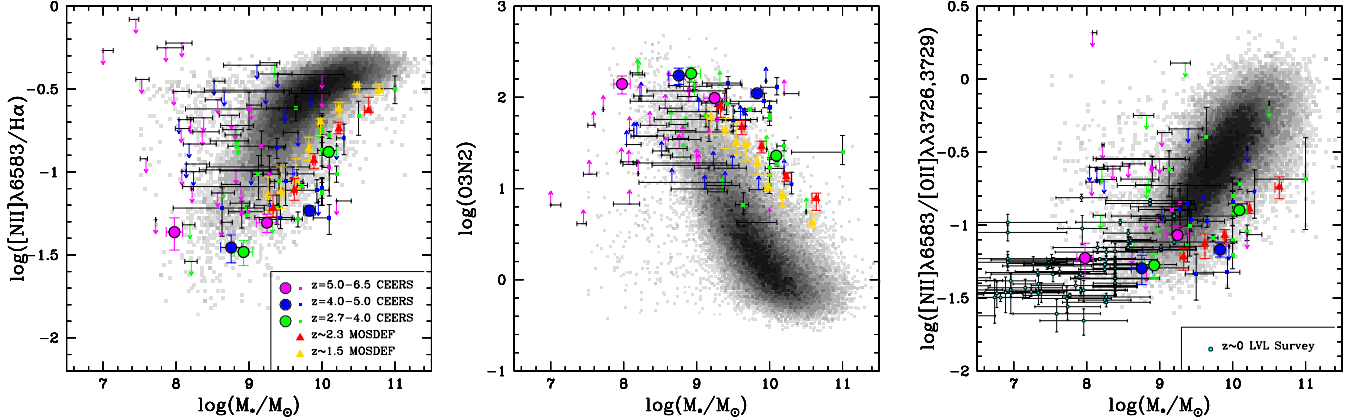


Figure 3. Nitrogen-related emission-line ratios vs. stellar mass for CEERS galaxies. These panels show the line ratios $[\text{NII}]\lambda 6583/\text{H}\alpha$ (left), O3N2 (center), and $[\text{NII}]\lambda 6583/[\text{OII}]\lambda 3727$ (right) versus M_* . All of these ratios include the $[\text{NII}]\lambda 6583$ feature commonly used to probe ISM conditions at $z \leq 2.5$. In each panel, the background grayscale histogram corresponds to the distribution of local SDSS star-forming galaxies. Individual CEERS galaxies are color-coded as in Figure 1, and indicated as small squares for detections or downward-facing (upward-facing) arrows for upper (lower) limits. Measurements from stacked CEERS spectra are indicated as large circles with the same color-coding as individual measurements. Measurements from stacked spectra of galaxies in the MOSDEF survey at $z \sim 1.5$ (Topping et al. 2021) and $z \sim 2.3$ (Sanders et al. 2021) are shown, respectively, with large gold and red triangles. In the right panel ($[\text{NII}]\lambda 6583/[\text{OII}]\lambda 3727$), we overplot low-mass galaxies from the Local Volume Legacy (LVL) Survey (Berg et al. 2012) with small cyan symbols, in order to indicate the regime of primary nitrogen enrichment in which N/O is independent of metallicity.

sistent with the scaling observed by Sanders et al. (2021) for $z \sim 2.3$ star-forming galaxies in the MOSDEF survey. On the other hand, MOSDEF star-forming galaxies at $z \sim 1.5$ show a progression towards higher $[\text{NII}]\lambda 6583/\text{H}\alpha$ at fixed stellar mass, which continues to $z \sim 0$. At $z \geq 4.0$, no strong trends are recovered between $[\text{NII}]\lambda 6583/\text{H}\alpha$ and stellar mass. In addition, the stellar mass range probed at $z > 5.0$ extends towards significantly lower values ($\log(M_*/M_\odot) \sim 8.0$). At this stellar mass, given the existence of the MZR, nitrogen production falls within the primary regime, as discussed below (and see Figure 14 of Andrews & Martini 2013).

O3N2 (Figure 3, center) and $[\text{NII}]\lambda 6583/[\text{OII}]\lambda 3727$ (Figure 3, right) tell a similar story, with the CEERS $z = 2.7-4.0$ sample overlapping the MOSDEF $z \sim 2.3$ scaling relations, and no strong trends within the CEERS $z > 4.0$ galaxies. One possible reason for the lack of strong scaling between $[\text{NII}]\lambda 6583/[\text{OII}]\lambda 3727$ and mass at $z > 4.0$ is that we are probing the low-metallicity regime of primary nitrogen production, where the N/O ratio is independent of metallicity (e.g., Pilyugin et al. 2012). Along these lines, in the panel displaying $[\text{NII}]\lambda 6583/[\text{OII}]\lambda 3727$ vs. M_* (Figure 3, right), we also plot low-mass galaxies from the Local Volume Legacy (LVL) Survey (Berg et al. 2012) that span the mass range probed by the $z = 5.0-6.5$ CEERS sample. At $\log(M_*/M_\odot) \leq 9.0$, and the corresponding $12 + \log(\text{O/H})$ values, there is no scaling between N/O and M_* in the $z \sim 0$ dwarf galaxies. Given the evolution of the MZR towards lower metallicity at fixed mass as redshift increases (e.g., Steidel et al. 2014; Kashino et al. 2017; Sanders et al. 2021), the CEERS $z = 5.0-6.5$ sample must represent an even lower

average metallicity at the same mass, and fall even more firmly within the primary nitrogen regime. More generally, if the $z > 4$ CEERS sample is indeed in the primary nitrogen regime while the $z < 3$ samples are not, this difference at least partially explains why $[\text{NII}]\lambda 6583/\text{H}\alpha$ and O3N2 have a flatter dependence on M_* in the $z > 4$ samples. However, such an explanation may not apply to the high-mass $z = 4.0-5.0$ bin, which is still significantly lower (higher) in $[\text{NII}]\lambda 6583/\text{H}\alpha$ (O3N2) than an interpolation of the $z = 2.7-4.0$ CEERS sample at the same M_* .

3.2. Line Ratios Including α Elements

We also consider several commonly studied ratios based on α elements (e.g. O, Ne): $[\text{OIII}]\lambda 5007/\text{H}\beta$, O_{32} , R_{23} , and $[\text{NeIII}]\lambda 3869/[\text{OII}]\lambda 3727$. The majority of galaxies in the CEERS $z = 2.7-6.5$ sample are detected in $[\text{OIII}]\lambda 5007/\text{H}\beta$, O_{32} , and R_{23} , although individual detections of the fainter $[\text{NeIII}]\lambda 3869$ line are achieved for only $\sim 40\%$ of the sample. As in earlier works (e.g., Juneau et al. 2014; Coil et al. 2015; Holden et al. 2016), we find an elevated $[\text{OIII}]\lambda 5007/\text{H}\beta$ at fixed stellar mass, relative to the local relation (Figure 4, top left). We also find a lack of significant evolution in $[\text{OIII}]\lambda 5007/\text{H}\beta$ at fixed stellar mass beyond $z \sim 3$. Specifically (with the exception of the high-mass bin at $z = 4.0-5.0$), the CEERS emission-line measurements at $z > 2.7$ are consistent with those from the MOSDEF $z \sim 3.3$ sample where they overlap in stellar mass.

While the bulk of $z > 1$ measurements shown here follow a trend of increasing $[\text{OIII}]\lambda 5007/\text{H}\beta$ as stellar mass decreases, at the lowest masses probed by individual galaxies

in the CEERS $z = 5.0 - 6.5$ sample, we find evidence of a turnover towards lower $[\text{OIII}]\lambda 5007/\text{H}\beta$. Specifically, several galaxies at the low-mass end of the CEERS sample fall significantly below the SDSS distribution in $[\text{OIII}]\lambda 5007/\text{H}\beta$ vs. M_* , whereas, above $\log(M_*/M_\odot) \sim 9.0$, we find only one such galaxy. The turnover is also suggested by the trends in the stacked datapoints from both CEERS and MOSDEF. Together, the CEERS and MOSDEF stacked datapoints trace a monotonically-decreasing sequence in $[\text{OIII}]\lambda 5007/\text{H}\beta$ as mass increases above $\log(M_*/M_\odot) \sim 9.0$. The CEERS low-mass $z = 5.0 - 6.5$ stack is characterized by a significantly lower mass ($\log(M_*/M_\odot) = 7.98$) and yet its $[\text{OIII}]\lambda 5007/\text{H}\beta$ value is identical to that of the CEERS low-mass stacks at $z = 2.7 - 4.0$ and $z = 4.0 - 5.0$. Such a turnover towards decreasing $[\text{OIII}]\lambda 5007/\text{H}\beta$ with decreasing mass at stellar masses below $\log(M_*/M_\odot) \sim 9.0$ is expected, given the relationship between $[\text{OIII}]\lambda 5007/\text{H}\beta$ and $12 + \log(\text{O/H})$ in this regime (Curti et al. 2020; Nakajima et al. 2022; Sanders et al. 2020). This turnover in $[\text{OIII}]\lambda 5007/\text{H}\beta$ at low stellar mass is also detected by Matthee et al. (2022) in *JWST*/NIRCam grism observations of a sample of $z \sim 6$ [OIII]-emitting galaxies.

Like $[\text{OIII}]\lambda 5007/\text{H}\beta$, the ratio O_{32} shows no significant evolution at $z \sim 3$ and beyond (Figure 4, top right). O_{32} is most directly sensitive to ionization parameter, and, through the anti-correlation between ionization parameter and oxygen abundance (Pérez-Montero 2014), indirectly traces metallicity (Sanders et al. 2016, 2018). As in the case of $[\text{OIII}]\lambda 5007/\text{H}\beta$, we find that CEERS galaxies at $z = 2.7 - 6.5$ generally have similar O_{32} to those in the $z \sim 3.3$ MOSDEF sample at fixed stellar mass.

As in the $[\text{NII}]\lambda 6583/\text{H}\alpha$ and O3N2 diagrams, the high-mass $z = 4.0 - 5.0$ bin presents as an outlier towards significantly higher $[\text{OIII}]\lambda 5007/\text{H}\beta$ and O_{32} at fixed stellar mass relative to the lower-redshift samples (there is no $z = 5.0 - 6.5$ data point in a similar mass range). We require a larger sample, deeper spectroscopy, and robustly-calibrated direct metallicity measurements at $z = 4.0 - 5.0$ (Sanders et al. 2023a) to determine whether this offset is truly representative of star-forming galaxies at this redshift, and reflective of higher-excitation physical conditions or else individually-undetected AGN activity in some sources.

In the space of R_{23} vs. stellar mass (Figure 4, bottom left), galaxies at $z \geq 2.3$ are offset from the local sequence towards higher R_{23} at fixed stellar mass, yet there is no evolution from $z \sim 2.3$ to $z = 6.5$ given that the MOSDEF $z \sim 2.3$ and $z \sim 3.3$ stacks follow the same relation. This behavior differs slightly from what is observed for $[\text{OIII}]\lambda 5007/\text{H}\beta$ (and O_{32}), where there is slight evolution towards higher line ratio ($\sim 0.1 - 0.2$ dex) at fixed mass between $z \sim 2.3$ and $z \sim 3.3$, and then no further evolution at higher redshift.

Finally, we find that $[\text{NeIII}]\lambda 3869/[\text{OII}]\lambda 3727$ shows evidence of being significantly higher at fixed stellar mass for CEERS galaxies at $z \geq 4$ than MOSDEF galaxies at $z \sim 3.3$ (and $z \sim 2.3$). Where we can most robustly gauge this offset, i.e., at $\log(M_*/M_\odot) \sim 9.0$ and excluding the CEERS high-mass $z = 4.0 - 5.0$ bin, we find that the the average offset in $[\text{NeIII}]\lambda 3869/[\text{OII}]\lambda 3727$ between CEERS $z \geq 4.0$ galaxies and MOSDEF $z \sim 3.3$ galaxies is +0.2 dex. At lower masses, there are no average measurements from the MOSDEF survey, so it is not possible to perform a similar comparison. We defer further interpretation of the behavior of $[\text{NeIII}]\lambda 3869/[\text{OII}]\lambda 3727$ at these low masses, as we require larger samples at both $z \geq 4$, and $z \sim 2 - 3$. We do note that, given the close proximity of the constituent lines in the $[\text{NeIII}]\lambda 3869/[\text{OII}]\lambda 3727$ ratio, the estimate of $[\text{NeIII}]\lambda 3869/[\text{OII}]\lambda 3727$ is immune to the uncertainties in dust correction and wavelength-dependent flux calibration associated with line ratios widely spaced in wavelength such as O_{32} and R_{23} . At the same time, the divergent behavior of O_{32} and $[\text{NeIII}]\lambda 3869/[\text{OII}]\lambda 3727$ as a function of redshift will require further investigation. Indeed, both ratios are sensitive to the ionization parameter, and both trace α elements (Strom et al. 2017; Witstok et al. 2021), so similar redshift evolution might have been expected. An elevated ratio of $[\text{NeIII}]\lambda 3869$ to $[\text{OIII}]\lambda 5007$ at $z > 4$ may be indicative of a harder ionizing spectrum (Jeong et al. 2020) at fixed nebular metallicity, or higher abundance ratio of neon to oxygen. The former possibility, however, is inconsistent with the conclusions of Sanders et al. (2023b) that the ionization conditions do not strongly evolve in CEERS galaxies from $z \sim 2$ to $z \sim 6$. The latter possibility also appears unlikely given the similar enrichment channels of neon and oxygen, and the lack of significant variation in Ne/O detected in local star-forming galaxies as a function of either metallicity or specific SFR (Izotov et al. 2006).

4. DISCUSSION

We have presented a systematic analysis of the empirical relationships between nebular emission-line ratios and stellar mass at $z = 2.7 - 6.5$, based on both individual and stacked composite *JWST*/NIRSpec spectra from the CEERS program (Finkelstein et al. 2023, 2022). We analyze common rest-optical line ratios (but some observed for the very first time at $z \geq 3$) based on nitrogen, α elements (oxygen, neon), and hydrogen. Though $[\text{NII}]\lambda 6583$ proves challenging to detect in individual galaxies at $z \geq 3$, we find based on stacked spectra that there is no strong evolution in the scaling of $[\text{NII}]\lambda 6583/\text{H}\alpha$, O3N2 , or $[\text{NII}]\lambda 6583/[\text{OII}]\lambda 3727$ with stellar mass, relative to measurements from the MOSDEF survey at $z < 3$ in an overlapping stellar mass range. At the lowest masses covered by the CEERS $z = 4.0 - 5.0$ and $z = 5.0 - 6.5$ samples, we furthermore find evidence for prob-

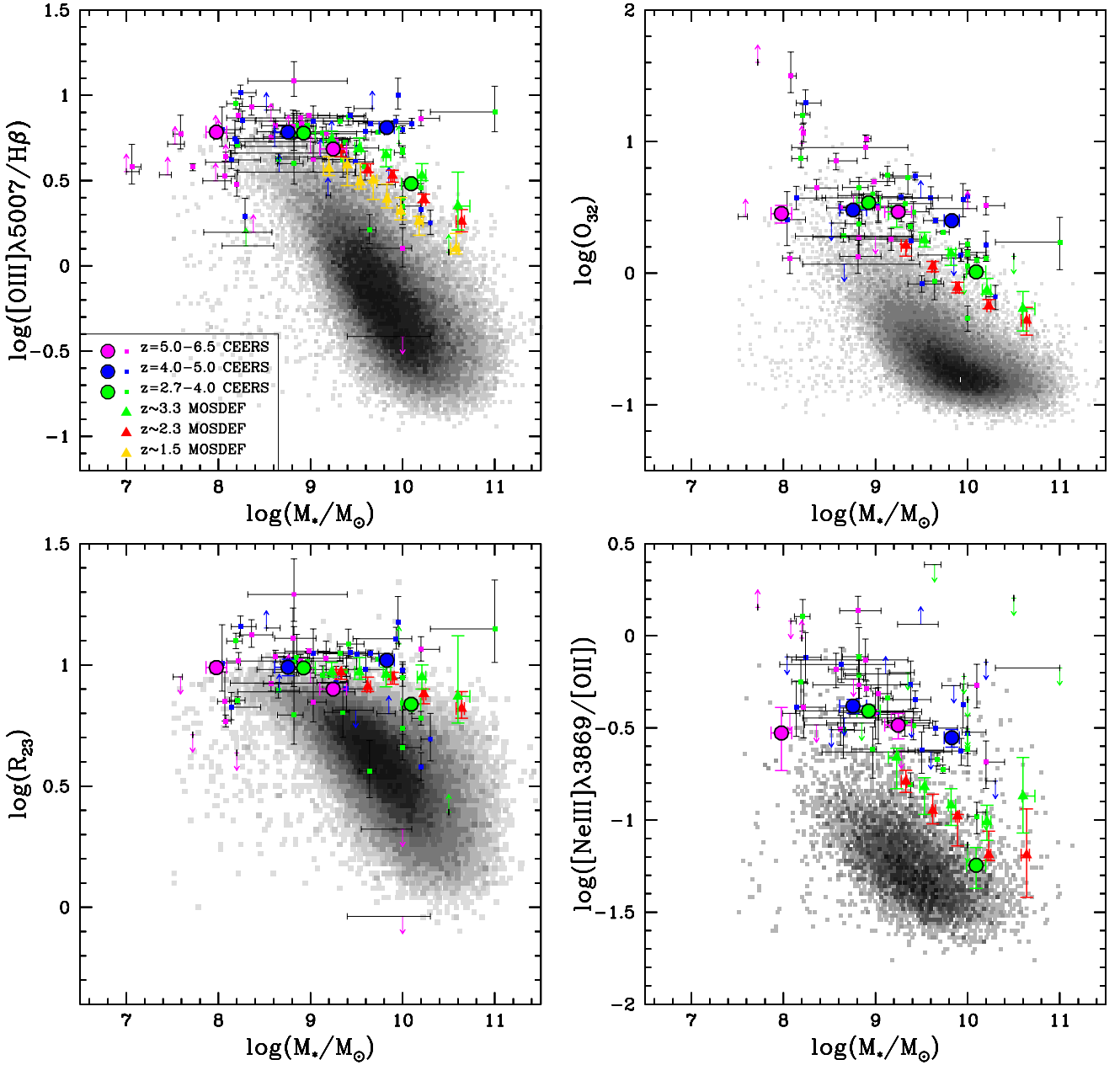


Figure 4. α -related emission-line ratios vs. stellar mass for CEERS galaxies. These panels shows the line ratios $[\text{OIII}]\lambda 5007$ (top left), O_{32} (top right), R_{23} (bottom left), and $[\text{NeIII}]\lambda 3869/[\text{OII}]\lambda 3727$ (bottom right). Symbols are as in Figure 3. In addition, measurements from stacked spectra of galaxies in the MOSDEF survey at $z \sim 3.3$ (Sanders et al. 2021) are shown with large green triangles.

ing a regime of primary nitrogen production. In terms of the α elements, we find no strong evolution at fixed mass beyond $z \sim 3$, in line ratios based on $[\text{OII}]\lambda 3727$ and $[\text{OIII}]\lambda 5007$. The empirical nebular emission-line ratios presented here are commonly translated into gas-phase metallicities in order to construct galaxy metallicity scaling relations (e.g., Tremonti et al. 2004; Sanders et al. 2021), and yet care must be taken when doing so. Specifically, robust calibrations are required for the translation between emission-line ratio and metallicity, and the calibrations adopted for local star-forming galax-

ies need to be updated for distant galaxies (e.g., Bian et al. 2018; Sanders et al. 2023a). We defer the actual translation between line ratio and metallicity to future work, but review here some recent attempts to use *JWST* to infer distant galaxy chemical abundances, and the reasons why such analyses are so important for constraining models of galaxy formation.

In addition to detailed investigations of remarkable individual NIRSpec spectra at high redshift (e.g., Curti et al. 2023; Williams et al. 2022; Bunker et al. 2023), *JWST* spectra are also starting to be used for analysis of the chemical abun-

dances of samples of distant galaxies. [Matthee et al. \(2022\)](#) present NIRCam grism observations of [OIII]/H β in concert with stellar mass estimates for a sample of 117 [OIII]-emitting galaxies at $5.3 \leq z \leq 6.9$. Metallicities are estimated from stacked spectra of galaxies in four bins of stellar mass using a single metallicity indicator, the [OIII]/H β ratio, because of the limited wavelength coverage of the NIRCam grism (i.e., $3-4\mu\text{m}$). It is worth noting both that there is very little variation in average [OIII]/H β across the four stellar mass bins, given that the galaxies in the [Matthee et al. \(2022\)](#) sample probe the peak of the [OIII]/H β distribution, and, further, that the metallicities inferred from [OIII]/H β are significantly higher at fixed mass than that inferred from a composite spectrum of $z = 6.25-6.90$ [OIII] emitters in which the auroral [OIII] $\lambda 4363$ line is detected. It will be important to estimate metallicities for this redshift range based on multiple emission-line ratios like those featured in the current work, including those that vary monotonically with metallicity (e.g., O₃₂, [NeIII] $\lambda 3869$ /[OII] $\lambda 3727$, O3N2), and using calibrations based on direct metallicities at high redshift.

More directly related to the current work, [Nakajima et al. \(2023\)](#) attempt to constrain the MZR at $z \sim 4-9$ with *JWST*/NIRSpec observations of a sample of 135 galaxies drawn from the publicly available CEERS, GLASS, and ERO programs. Gas-phase metallicities are primarily based on R₂₃ (78 galaxies) or [OIII] $\lambda 5007$ /H β (49 galaxies), with an additional 8 galaxies having direct T_e -based metallicities. Consistent with our empirical results, [Nakajima et al. \(2023\)](#) find only weak evolution in the MZR between $z \sim 2-3$ and $z \sim 4-9$. However, we caution that [Nakajima et al. \(2023\)](#) have SED-based stellar mass estimates for 81 galaxies in their *JWST* metallicity sample. The remaining 54 galaxies have stellar mass estimates (31 galaxies) or upper limits (23 galaxies) inferred from UV luminosities alone, which carry significant uncertainties due to variations in the mass-to-light ratio. Furthermore, additional work is needed to establish robust metallicity calibrations at $z > 3$ based on a larger sample of direct T_e -based metallicities at high redshift.

With proper calibration from direct metallicities (e.g., [Curti et al. 2023; Sanders et al. 2023b](#)), *JWST* promises to provide excellent observational constraints on the evolution of the MZR at $z > 3$. With a large enough sample and robust SFR estimates, it will also be possible to determine the nature of the FMR among oxygen abundance, M_{*}, and SFR, and whether it remains as invariant at higher redshift as it does from $z \sim 0$ to $z \sim 3.3$ ([Sanders et al. 2021](#)). In order to determine the evolution of the MZR, which is meant to represent the average properties of star-forming galaxies at different cosmic epochs, it will be necessary to assemble not only large but also *representative* galaxy samples. As discussed in [Shapley et al. \(2023\)](#), the CEERS galaxies we analyze here appear representative of the star-forming main sequence at

$z = 2.7-5.0$, but with higher-than-average sSFR at $z > 5.0$. Given the connections among oxygen abundance, M_{*}, and SFR, we also require star-forming galaxy samples at $z > 5.0$ that are representative in SFR at fixed M_{*}, if we aim to trace MZR evolution at $z > 5.0$.

Observational MZR constraints can be compared with theoretical predictions for the evolution of the MZR at the earliest times. For example, predictions in the literature for this evolution vary considerably. Both [Torrey et al. \(2019\)](#), based on the IllustrisTNG simulations, and [Ma et al. \(2016\)](#), based on the FIRE simulations, predict evolution of ~ -0.3 dex in gas-phase metallicity at fixed stellar mass from $z = 3$ to $z \sim 6$ as galaxy gas fractions increase, though the normalization of the MZR is significantly higher in [Torrey et al. \(2019\)](#). Furthermore, [Torrey et al. \(2019\)](#) predict a linear decline in 12+log(O/H) with increasing redshift, whereas [Ma et al. \(2016\)](#) predict a flattening in the evolution of the MZR with increasing redshift. In contrast, at slightly higher redshift ($z = 5-8$) and based on the FirstLight simulations, [Langan et al. \(2020\)](#) predict weak evolution in the normalization of the MZR. The evolution detected in this model is actually towards *increasing* metallicity with increasing redshift, since galaxy gas reservoirs are described to build up with time (decreasing redshift) over this interval, as gas accretion outpaces star formation and outflows. Furthermore, while the predicted MZR evolution from [Ma et al. \(2016\)](#) is also very shallow within this higher redshift range, the MZR normalization from FIRE is ~ 0.3 dex lower than in the FirstLight simulations.

Differences among galaxy formation model predictions arise because of how the processes of gas inflow, build-up, and outflow are described ([Langan et al. 2020](#)). Accordingly, robust measurements of the evolution of the MZR with *JWST* will be able to distinguish among the different prescriptions for baryon cycling at early times. In its first months, *JWST* has demonstrated that it is capable of returning the necessary data to trace the MZR at $z > 3$. We now need to assemble sufficient sample sizes (a factor of several larger than the CEERS/NIRSpec $z > 3$ sample) with both strong emission-line and stellar mass measurements, and an adequate direct T_e -based-metallicity calibration sample for translating emission-line ratios into metallicities.

ACKNOWLEDGEMENTS

We acknowledge the entire CEERS team for their effort to design and execute this Early Release Science observational program, especially the work to design the MSA observations. This work is based on observations made with the NASA/ ESA/CSA James Webb Space Telescope. The data were obtained from the Mikulski Archive for Space Telescopes at the Space Telescope Science Institute, which is operated by the Association of Universities for Research

in Astronomy, Inc., under NASA contract NAS5-03127 for JWST. The specific observations analyzed can be accessed via DOI: [10.17909/z7p0-8481](https://doi.org/10.17909/z7p0-8481). We also acknowledge support from NASA grant JWST-GO-01914. Support for this

work was also provided through the NASA Hubble Fellowship grant #HST-HF2-51469.001-A awarded by the Space Telescope Science Institute, which is operated by the Association of Universities for Research in Astronomy, Incorporated, under NASA contract NAS5-26555.

REFERENCES

Abazajian, K. N., Adelman-McCarthy, J. K., Agüeros, M. A., et al. 2009, *ApJS*, 182, 543

Andrews, B. H., & Martini, P. 2013, *ApJ*, 765, 140

Arellano-Córdova, K. Z., Berg, D. A., Chisholm, J., et al. 2022, *ApJL*, 940, L23

Berg, D. A., Skillman, E. D., Marble, A. R., et al. 2012, *ApJ*, 754, 98

Bian, F., Kewley, L. J., & Dopita, M. A. 2018, *ApJ*, 859, 175

Bunker, A. J., Saxena, A., Cameron, A. J., et al. 2023, arXiv e-prints, arXiv:2302.07256

Cameron, A. J., Saxena, A., Bunker, A. J., et al. 2023, arXiv e-prints, arXiv:2302.04298

Cardelli, J. A., Clayton, G. C., & Mathis, J. S. 1989, *ApJ*, 345, 245

Chabrier, G. 2003, *PASP*, 115, 763

Coil, A. L., Aird, J., Reddy, N., et al. 2015, *ApJ*, 801, 35

Conroy, C., Gunn, J. E., & White, M. 2009, *ApJ*, 699, 486

Curti, M., Mannucci, F., Cresci, G., & Maiolino, R. 2020, *MNRAS*, 491, 944

Curti, M., D'Eugenio, F., Carniani, S., et al. 2023, *MNRAS*, 518, 425

Ellison, S. L., Patton, D. R., Simard, L., & McConnachie, A. W. 2008, *ApJL*, 672, L107

Finkelstein, S. L., Bagley, M. B., Haro, P. A., et al. 2022, *ApJL*, 940, L55

Finkelstein, S. L., Bagley, M. B., Ferguson, H. C., et al. 2023, *ApJL*, 946, L13

Fujimoto, S., Arrabal Haro, P., Dickinson, M., et al. 2023, arXiv e-prints, arXiv:2301.09482

Holden, B. P., Oesch, P. A., González, V. G., et al. 2016, *ApJ*, 820, 73

Izotov, Y. I., Stasińska, G., Meynet, G., Guseva, N. G., & Thuan, T. X. 2006, *A&A*, 448, 955

Jeong, M.-S., Shapley, A. E., Sanders, R. L., et al. 2020, *ApJL*, 902, L16

Juneau, S., Bournaud, F., Charlot, S., et al. 2014, *ApJ*, 788, 88

Kashino, D., Silverman, J. D., Sanders, D., et al. 2017, *ApJ*, 835, 88

Kriek, M., van Dokkum, P. G., Labbé, I., et al. 2009, *ApJ*, 700, 221

Langan, I., Ceverino, D., & Finlator, K. 2020, *MNRAS*, 494, 1988

Langeroodi, D., Hjorth, J., Chen, W., et al. 2022, arXiv e-prints, arXiv:2212.02491

Ma, X., Hopkins, P. F., Faucher-Giguère, C.-A., et al. 2016, *MNRAS*, 456, 2140

Mannucci, F., Cresci, G., Maiolino, R., Marconi, A., & Gnerucci, A. 2010, *MNRAS*, 408, 2115

Mascia, S., Pentericci, L., Calabro, A., et al. 2023, *A&A*, 672, A155

Matthee, J., Mackenzie, R., Simcoe, R. A., et al. 2022, arXiv e-prints, arXiv:2211.08255

Nakajima, K., Ouchi, M., Isobe, Y., et al. 2023, arXiv e-prints, arXiv:2301.12825

Nakajima, K., Ouchi, M., Xu, Y., et al. 2022, *ApJS*, 262, 3

Onodera, M., Carollo, C. M., Lilly, S., et al. 2016, *ApJ*, 822, 42

Pérez-Montero, E. 2014, *MNRAS*, 441, 2663

Pilyugin, L. S., Grebel, E. K., & Mattsson, L. 2012, *MNRAS*, 424, 2316

Reddy, N. A., Topping, M. W., Sanders, R. L., Shapley, A. E., & Brammer, G. 2023, arXiv e-prints, arXiv:2301.07249

Reddy, N. A., Shapley, A. E., Kriek, M., et al. 2020, *ApJ*, 902, 123

Sanders, R. L., Shapley, A. E., Topping, M. W., Reddy, N. A., & Brammer, G. B. 2023a, arXiv e-prints, arXiv:2303.08149

—. 2023b, arXiv e-prints, arXiv:2301.06696

Sanders, R. L., Shapley, A. E., Kriek, M., et al. 2016, *ApJ*, 816, 23

—. 2018, *ApJ*, 858, 99

Sanders, R. L., Shapley, A. E., Reddy, N. A., et al. 2020, *MNRAS*, 491, 1427

Sanders, R. L., Shapley, A. E., Jones, T., et al. 2021, *ApJ*, 914, 19

Shapley, A. E., Sanders, R. L., Reddy, N. A., Topping, M. W., & Brammer, G. B. 2023, arXiv e-prints, arXiv:2301.03241

Speagle, J. S., Steinhardt, C. L., Capak, P. L., & Silverman, J. D. 2014, *ApJS*, 214, 15

Steidel, C. C., Rudie, G. C., Strom, A. L., et al. 2014, *ApJ*, 795, 165

Strom, A. L., Steidel, C. C., Rudie, G. C., et al. 2017, *ApJ*, 836, 164

Tang, M., Stark, D. P., Chen, Z., et al. 2023, arXiv e-prints, arXiv:2301.07072

Topping, M. W., Shapley, A. E., Sanders, R. L., et al. 2021, *MNRAS*, 506, 1237

Torrey, P., Vogelsberger, M., Marinacci, F., et al. 2019, *MNRAS*, 484, 5587

Tremonti, C. A., Heckman, T. M., Kauffmann, G., et al. 2004, *ApJ*, 613, 898

Williams, H., Kelly, P. L., Chen, W., et al. 2022, arXiv e-prints, arXiv:2210.15699

Witstok, J., Smit, R., Maiolino, R., et al. 2021, MNRAS, 508, 1686